Single crystalline $CH_3NH_3PbI_3$ self-grown on FTO/TiO_2 substrate for high efficiency perovskite solar cells

Jinjin Zhao[1,2,*] , Guoli Kong[1], Shulin Chen[3,8], Qian Li[4] , Boyuan Huang[2,5], Zhenghao Liu[2], Xingyuan San[6], Yujia Wang[6], Chen Wang[1], Yunce Zhen[1], Haidan Wen[4], Peng Gao[3,7], Jiangyu Li[2,5,*]

1. School of Materials Science and Engineering, Shijiazhuang Tiedao University, Shijiazhuang, 050043, China
2. Shenzhen Key Laboratory of Nanobiomechanics, Shenzhen Institutes of Advanced Technology, Chinese Academy of Sciences, Shenzhen 518055, Guangdong, China
3. Electron Microscopy Laboratory, and International Center for Quantum Materials, School of Physics, Peking University, Beijing 100871, China
4. X-ray Science Division, Argonne National Laboratory, Lemont IL, 60439, USA
5. Department of Mechanical Engineering, University of Washington, Seattle, WA 98195-2600, USA
6. Shenyang National Laboratory for Materials Science (SYNL), Institute of Metal Research, Chinese Academy of Sciences, Wenhua Road 72, 110016 Shenyang, China
7. Collaborative Innovation Center of Quantum Matter, Beijing 100871, China
8. State Key Laboratory of Advanced Welding and Joining, Harbin Institute of Technology, Harbin 150001, China

Abstract

In this work, we developed an innovative approach to self-grow single crystalline $CH_3NH_3PbI_3$ directly on polycrystalline FTO/TiO_2 substrate, with which n-i-p type of perovskite solar cells were fabricated. The single crystalline nature of $CH_3NH_3PbI_3$ has been confirmed by X-ray diffraction and high resolution transmission electron microscopy, and it is observed that they possess smaller optic band gap and longer carrier life time. Highly efficient charge extractions occur at the interface between electron collecting TiO_2 and photo-harvesting $CH_3NH_3PbI_3$, resulting in a maximum short-circuit current density of 24.40 mA/cm^2. The champion cell possesses a photovoltaic conversion efficiency of 8.78%, and there are still substantial room for further improvement, making it promising for the perovskite solar cell applications.

* Authors to whom the correspondence should be addressed to; Email: jinjinzhao2012@163.com and jjli@uw.edu.

Introduction

Since its first report in 2009 [1], $CH_3NH_3PbI_3$-based perovskite solar cells (PSCs) have emerged as one of the most exciting developments in the next generation photovoltaic (PV) technologies [2–4], with its PV conversion efficiency (PCE) rising spectacularly from 3.81% to 22.1% in just 7 years [5–8]. Such rapid advance is unprecedented in any other PV systems, which has fueled intense competitions for its PCE record worldwide. While still far away from its theoretical limit [9], the recent PCE advances in PSCs have slowed down considerably, due to the inevitable defects associated with grains and grain boundaries in polycrystalline perovskites as well as their poor stability. It is thus not surprising that some of recent efforts in PSCs have been shifted toward developing single crystalline perovskite materials.

Initial efforts in single crystalline PSCs have been focused on growing large crystals of $CH_3NH_3PbI_3$ and related materials, which has resulted in observations of carrier diffusion length exceeding 175 μm and carrier life time over 262 μs, thanks to much reduced trap state density in single crystals [10–12]. Such exceptional photo-carrier properties of single crystalline perovskites, however, have yet to be translated into gains in their PCEs, since it is rather difficult to integrate single crystals of $CH_3NH_3PbI_3$ and related materials into the device architecture of PSCs, wherein interfaces between the photo-harvesting perovskites and carrier collectors such as TiO_2 are critical. For example, large crystalline wafer of perovskite has been sliced into thin layers to make optoelectronic devices [13,14], though the corresponding solar cell has a relatively low short-circuit current density (J_{sc}) of 13.5 mA/cm^2, resulting in single crystalline PCEs around 4%. Meanwhile, patterned wafer-scale single crystalline film of $CH_3NH_3PbI_3$ processed via geometrically-confined lateral crystal growth has also been reported, exhibiting PCE of 4.83% recorded in a PSC with a lateral configuration [15]. Furthermore, single crystalline $CH_3NH_3BrI_3$ films have also been developed using space-limited inverse temperature crystallization (SLITC)

growth, resulting in the highest PCE of 7.11% reported to date among single crystalline PSCs [16]. While still not comparable to the PCEs of polycrystalline PSCs, these recent successes underscore the great potential of single crystalline perovskites in the next generation PV applications.

Here, we report a new strategy to self-grow high quality single crystalline perovskite $CH_3NH_3PbI_3$ directly on electron-collecting FTO(F:SnO_2)/TiO_2 substrate, making its integration into PSC device architecture straightforward. The single crystalline structure of $CH_3NH_3PbI_3$ as grown has been examined by X-ray diffraction (XRD) and transmission electron microscopy (TEM), thanks to their excellent quality and high stability. More importantly, it is observed that the single crystalline perovskite possesses long carrier life time and highly efficient electron collection at the interface with TiO_2, leading to the highest single crystalline PCE of 8.78% recorded to date, to our best knowledge. It is further noted that such efficiency is accomplished without the single crystalline perovskite fully covering FTO/TiO_2 substrate, suggesting that its intrinsic PCE is even higher, and there are still substantial room for further improvement.

Experimental Methods

Following the processes reported in literatures, CH_3NH_3I was synthesized [17], and FTO/TiO_2 substrate was prepared [6]. Two pieces of FTO/TiO_2 substrates were then clamped together by the fixed size card slots. 2 mL of 1.3 mol/L precursor solution of PbI_2/CH_3NH_3I with a molar ratio of 1:1 were prepared in γ-butyrolactone and filtered using Polytetrafluoroethylene (PTFE) filter with 200 μm pore size. The clamped FTO/TiO_2 substrates were then vertically dipped into a 10 mL beaker containing $CH_3NH_3PbI_3$ precursor solution kept on a hot plate at 120 ^oC, and the feeding precursor solution was added once every 12 hours. After certain period, the substrates with self-grown film were taken out, washed by diethyl ether, and dried at 120^oC for

20min. The perovskite $CH_3NH_3PbI_3$ as grown were then characterized, or used for subsequent fabrication of n-i-p type PSC devices following a procedure reported elsewhere [18].

The morphologies of the $CH_3NH_3PbI_3$ sample were exampled by scanning electron microscopy (SEM, ZEISS GeminiSEM 300) and atomic force microscopy (AFM, Asylum Research Cypher ES). Electron backscatter diffraction (EBSD) Kikuchi patterns was obtained on Oxford NordlysMax2 detector and analyzed using AZtecHKL software. Powder XRD patterns were obtained on D8 Advance diffractometer using Cu Kα radiation (40 kV and 40 mA) with the scanning rate of $4°min^{-1}$ for wide angle test increment. X-ray photoelectron spectroscopy (XPS) was conducted using an ESCALAB250 spectrometer equipped with a monochromatized Al K source.

Single crystal X-ray diffraction was performed at the Sector 7-ID-C beamline of the Advanced Photon Source, Argonne National Laboratory. The primary X-ray beam with an energy of 10 keV was selected from a diamond-(111) double crystal monochromator with its size defined by a 300×300 μm^2 slit. A Huber six-circle diffractometer coupled with a PILATUS 100K area detector was employed for alignment of the single-crystalline samples and measurement of both specular and off-specular reflections. The detector was placed downstream from the samples such that ~8° coverage in the 2θ-angle and ~3° in the χ-angle was obtained. Rocking (ω-angle) scans around each reflection were recorded and typically, resultant 3D data volume was reduced by the χ-projection for data analysis.

High resolution TEM (HRTEM), scanning transmission electron microscopy (STEM) images and Energy dispersive X-Ray spectroscopy (EDX) mappings were acquired at an aberration-corrected TEM (Titan Cubed Themis G2, FEI) operated at 80 kV. The TEM samples were prepared in an argon-filled glovebox to avoid side reactions. The samples were firstly

scratched from substrate and dispersed into anhydrous ether with manual shake for about 2 minutes. Then, the clear suspensions were deposited on holey carbon copper girds for TEM characterizations. Low-magnification and high-resolution TEM images were also recorded using a conventional TEM (Tecnai G2 F30 FEI) under 300 kV, as presented in the Supplementary Information (SI).

Ultraviolet (UV) absorption spectra were obtained using Hitachi (U-4100). The steady-state photoluminescence (PL) and time-resolved photoluminescence (TRPL, with excitation light of 400 nm) were measured via Edinburgh Instruments LTD (FLS5). The photocurrent-voltage (*J–V*) characteristics of the solar cells were measured using a Keithley 2400 Source under illumination of a simulated sunlight (AM1.5, 100 mW cm^2) provided by a solar simulator (Newport 69907) with an AM 1.5 filter. Light intensity was adjusted with an NREL-calibrated Si solar cell with a KG-2 filter for approximating 1 sun light intensity. While measuring current and voltage, the cell was covered with a black mask with an aperture close to the active device area. The incident photon-to-current efficiency (IPCE) was measured in DC mode with a 1/4 m double monochromator (Crowntech DK242), a multi-meter (Keithley 2000), and two light sources (300–600 nm: xenon lamp, 300 W; 600–900 nm: tungsten-halogen lamp, 150 W). The monochromatic light intensity for IPCE was calibrated using a reference silicon photodiode.

Results and Discussions

The single crystalline $CH_3NH_3PbI_3$ was self-grown on the FTO/TiO_2 substrate, as schematically shown in Fig. 1(a), wherein the electron-collecting TiO_2 layer consists of mesoporous TiO_2 (m-TiO_2) on top of compact TiO_2 (c-TiO_2). The FTO/TiO_2 substrate was dipped vertically into the $CH_3NH_3PbI_3$ precursor solution with its temperature set at 120^{o}C, and another parallel FTO/TiO_2 glass, approximately 50-200 micrometers from the substrate using a

teflon spacer, was dipped into the precursor solution as well to form a controlled gap. The capillary pressure and temperature gradient drove the solution upward on the substrate, and the thickness of solution film depends on the gap size that could be adjusted. The growth also occurred on glass or on FTO substrate in the absence of m-TiO_2, though at much slower rate.

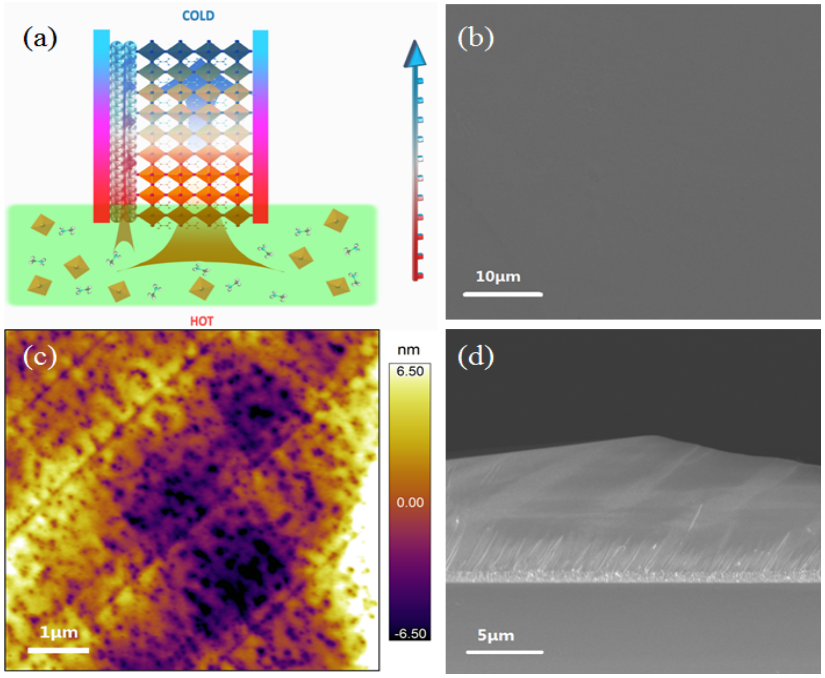

Fig. 1 Single crystalline $CH_3NH_3PbI_3$ self-grown on FTO/TiO_2 and glass substrates. **a** Schematic self-growth via temperature gradient and capillary effect. **b** Top view SEM image of $CH_3NH_3PbI_3$ on FTO/TiO_2. **c** AFM topography mapping of $CH_3NH_3PbI_3$ on glass. **d** Cross-sectional SEM image of $CH_3NH_3PbI_3$ on FTO/TiO_2.

After being taken out of the solution and annealed under 120°C for 20 minutes, large scale perovskite $CH_3NH_3PbI_3$ crystal with lateral size over several hundred micrometers was obtained, as shown by the top view and cross-sectional scanning electron microscopy (SEM) image in Fig. S1 of the SI. Higher magnification SEM image in Fig. 1(b) shows rather uniform crystal surface, and EBSD taken at four different spots reveal identical Kikuchi patterns (Fig. S1), demonstrating their identical crystallographic orientations characteristic of single crystal.

Mapping of AFM topography in Fig. 1(c) shows smooth surface with root mean square (RMS) roughness around 3.36 nm, and the line feature observed in AFM topography is deemed not an artifact, but may arise from domains of ferroelastic or ferroelectric nature [19–22], though its characteristics are still under investigation. Further details on the perovskite surface are shown by AFM topography of different scan sizes (Fig. S2), wherein the line feature is also observed in larger area. The cross-sectional SEM image in Fig. 1(d) reveals a tightly integrated interface between $CH_3NH_3PbI_3$ and FTO/TiO_2, which is important for the PSC devices. The grain features evident in TiO_2 layer is clearly absent in $CH_3NH_3PbI_3$, though the top surface appears uneven.

The crystallinity of $CH_3NH_3PbI_3$ sample was examined by X-ray diffraction over large surface region on the scale of hundreds of microns, and the results in Fig. 2 illustrate the profiles of several measured reflections denoted in the pseudo-cubic setting. All measured reflections appear to contain multiple split peaks, suggesting a lower-symmetry structure at room temperature. A total of 14 peak positions were extracted and indexed with the Dicvol06 program, yielding a highest-symmetry, orthorhombic unit cell with lattice parameters a = 6.322(4) Å, b = 6.287(2) Å and c = 6.273(2) Å averaged for the probed sample volume. The observation of 002_C-type reflections in the specular condition suggests that the dominant vertical growth direction of $CH_3NH_3PbI_3$ is along the $[001]_C$, and the full width at half maximum (FWHM) of the ω-rocking angle is found to be ~0.2°. The 002_C peaks observed at two distinct 2θ angles but almost identical ω-/χ-angles suggest their association with two types of vertical growth manners rather than the low-symmetry structure twinning. Despite this and the observed overlapping among non-specular reflections, a lack of powder diffraction clearly demonstrates the large, discreet single-crystalline nature of the $CH_3NH_3PbI_3$ sample. This is in contrast to the powder rings observed at 41.23°, 48.8° and a few other angles that arise from the polycrystalline TiO_2 layer, because the $CH_3NH_3PbI_3$ crystals do not fully cover the substrate, as shown by SEM image in Fig. S3, where

a few crystals as large as millimeter are seen on the substrate. The detailed in-plane alignment information of the sample is still under investigation, and the misalignment could explain the averaged orthorhombic structure that is slightly distorted from the usually reported tetragonal unit cell. We thus resort to TEM to examine the structure of a single $CH_3NH_3PbI_3$ crystal.

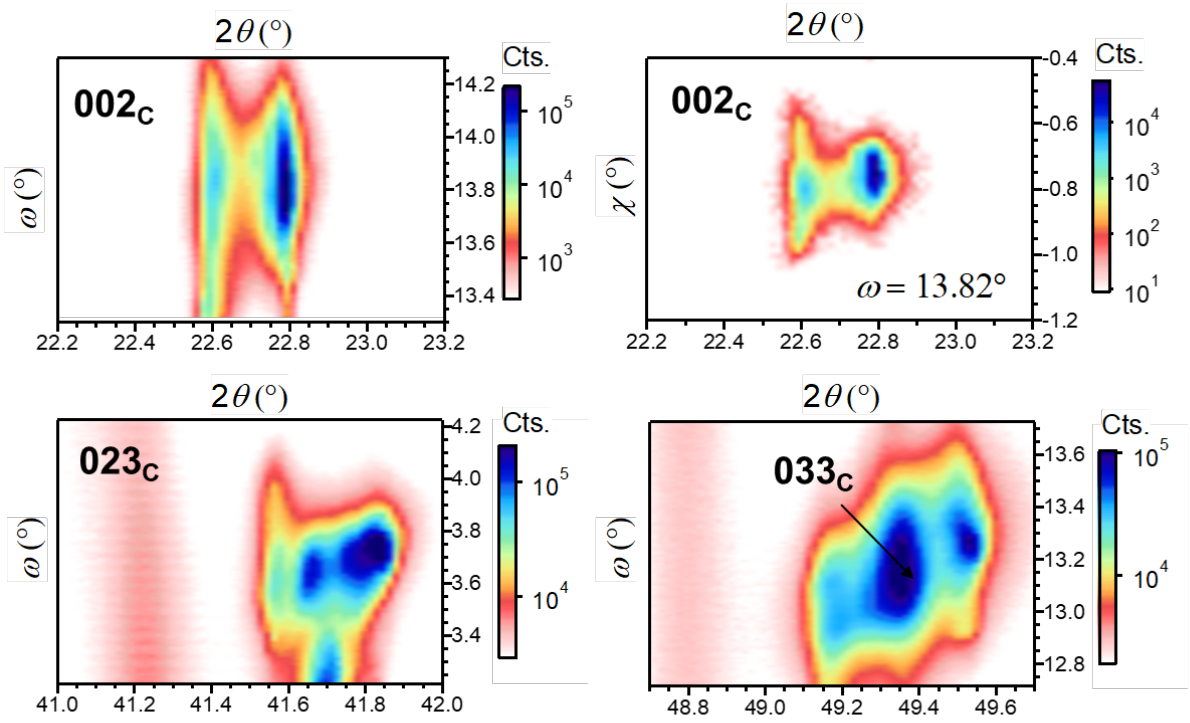

Fig. 2 Selected reflections measured from $CH_3NH_3PbI_3$ on FTO/TiO_2 substrate, indicating single crystalline structure. The powder rings at 41.23° and 48.8° arise from TiO_2.

Crystallography and elemental mapping of single crystalline $CH_3NH_3PbI_3$ were examined by HRTEM and EDX in STEM as shown in Fig. 3. Low resolution STEM image of $CH_3NH_3PbI_3$ (Fig. 3(a)) shows a regular polygon outlook, while HRTEM image (Fig. 3(b)) shows well-ordered crystalline lattice. The corresponding Fast Fourier transform (FFT) pattern (Fig. 3(c)) is identified to be tetragonal phase with viewing direction along the [210] zone axis, which is confirmed by the simulated electron diffraction pattern (Fig. 3(d)). The tetragonal phase is

consistent with previous report [23] as well as our own powder XRD pattern (Fig. S4). Single crystalline nature of the sample is further revealed by Fig. S5, wherein two separate areas of a 2 μm-long flake (Fig. S5(a)) show identical lattice planes (Fig. S5(b)) and selected area electron diffraction (SAED) patterns (Fig. S5(c)). EDX mappings of the sample in Fig. 3a indicate uniform distribution of C (Fig. 3(e)), N (Fig. 3(f)), Pb (Fig. 3(g)), and I (Fig 3(h)), respectively, and the presence of these elements are also confirmed by XPS (Fig. S6). The single crystalline nature of $CH_3NH_3PbI_3$ on FTO/TiO_2 is thus confirmed.

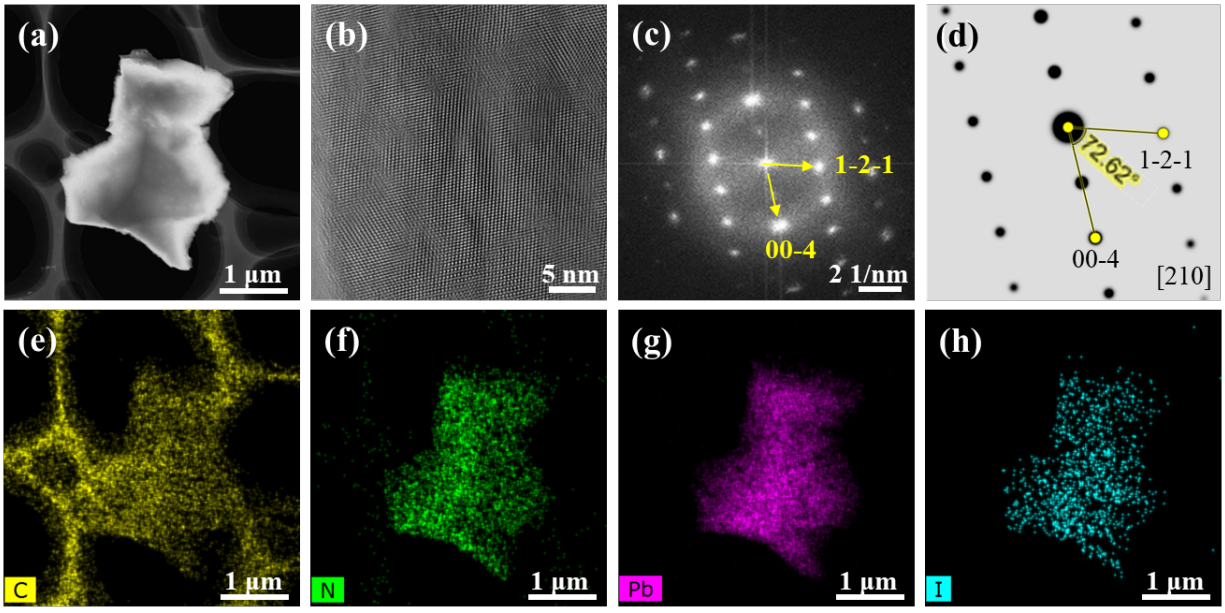

Fig. 3 Crystallography and EDX spectroscopy of single crystalline $CH_3NH_3PbI_3$. **a** STEM image. **b** HRTEM image. **c** Fast Fourier transform (FFT) pattern of (b). **d** Simulated electron diffraction pattern of tetragonal single crystal $CH_3NH_3PbI_3$ viewing along [210] direction. **e-h** Energy dispersive X-Ray (EDX) spectroscopy of C (e), N (f), Pb (g), and I (h), respectively.

To investigate the optic properties of the material, the UV-vis absorptions of both single- and poly-crystalline $CH_3NH_3PbI_3$ are compared in Fig. 4(a), where it is observed that the single crystalline perovskite exhibits an extended absorption band to 870 nm, whereas polycrystalline

one has an absorption cutoff at 780 nm. This leads to an estimated optic band gap of 1.50 eV for single crystalline $CH_3NH_3PbI_3$, compared to 1.57 eV for polycrystalline one (Fig. 4(b)), consistent with previous report [11]. Correspondingly, the steady PL of single crystalline perovskite red-shifts to 830 nm from 780 nm of polycrystalline one (Fig. 4(c)). In order to study exciton diffusion, we employed TRPL to compare the carrier lifetime in polycrystalline $CH_3NH_3PbI_3$ on FTO and single crystalline $CH_3NH_3PbI_3$ on FTO as well as on FTO/TiO_2, as shown in Fig. 4(d), monitored at the wavelength of 400 nm. In the absence of electron-collecting TiO_2, the longer carrier life time reflects higher exciton concentration and fewer recombination [24,25], which is what we observe in the single crystalline $CH_3NH_3PbI_3$ compared to the polycrystalline one, suggesting much reduced defects in the single crystal. When the single crystalline $CH_3NH_3PbI_3$ is deposited on the electron collecting FTO/TiO_2 substrate, on the other hand, the carrier life time is reduced substantially due to highly efficient electron extraction by TiO_2, thanks to its good interface with the single crystalline perovskite. Such comparison can be better appreciated by fitting the TRPL decay curves using double exponential equation [26] $I = I_0 + A_1 e^{-t/\tau_1} + A_2 e^{-t/\tau_2}$, with the corresponding fitting parameters listed in Table 1. It is found that the average carrier lifetime of 206.2 ns of single crystalline perovskite is 25.5 times longer than 8.1 ns of polycrystalline one, because exciton lifetime in polycrystal is deteriorated by grain boundaries and defects, which contributes to the increased electron transport resistance and bi-molecular recombination [27,28]. When put on the FTO/TiO_2 substrate, the carrier life time of the single crystal is reduced substantially to 11.2 ns because of efficient electron extraction at TiO_2/perovskite interface.[29,30]

Table 1 Parameters that fits to the TRPL measurement based on double exponential equation

Sample	τ_1/ns	A_1/%	τ_2/ns	A_2/%	Avg/ns
FTO/PC	4.1	80.5	24.7	19.5	8.1
FTO/SC	64.0	51.3	356.1	48.7	206.2
FTO/TiO_2/SC	1.1	0.7	11.3	99.3	11.2

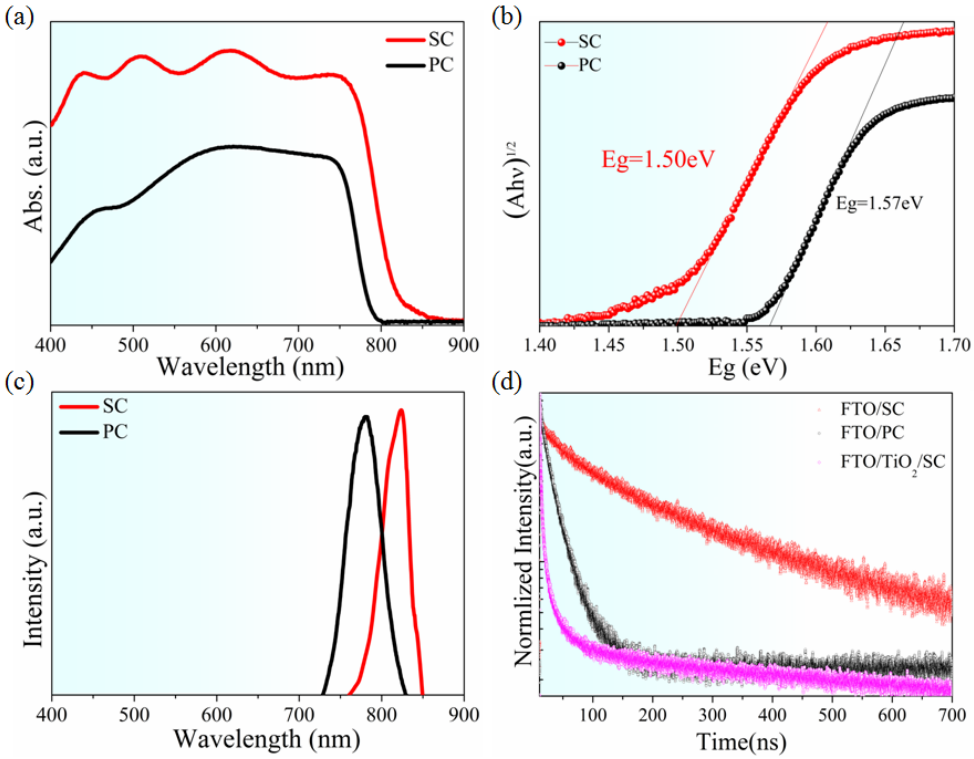

Fig. 4 Optic and photo-carrier properties of single crystalline (SC) and polycrystalline (PC) $CH_3NH_3PbI_3$. **a** UV-vis adsorption. **b** Optic band gap. **c** Steady PL. **d** TRPL.

The narrower band gap, higher exciton concentration with less recombination, and highly efficient electron extraction are expected to contribute significantly to the high J_{sc} for the single crystalline PSCs. Indeed, the n-i-p type PSCs consisting of FTO/TiO_2/$CH_3NH_3PbI_3$/Spiro-OmeTAD/Ag was fabricated, as shown by the cross-sectional SEM image in Fig. 5(a), by spin

coating Spiro-OmeTAD on FTO/TiO_2/$CH_3NH_3PbI_3$ as the hole transfer materials (HTM), followed by Ag evaporation. Fig. 5(b) shows the current-voltage characteristics (*J-V*) for the champion cell measured under simulated solar AM1.5G irradiation (100 $mWcm^{-2}$), revealing an open-circuit voltage (V_{oc}) of 0.67V, J_{sc} of 22.28 mA cm^{-2}, and a fill factor (FF) of 0.59, resulting in PCE of 8.78%, the highest reported among single crystalline PSCs to our best knowledge. Other 9 devices tested have PCE ranging from 6.14% to 8.21%, as shown in Table S1 with selected *J-V* curves in Fig. S7, where the maximum J_{sc} is observed to be 24.40 mA/cm^2. The IPCE spectrum of single crystalline PSC in Fig. 5(c) shows two peaks value of about 85.5% at 796nm and 77.0% at 861nm, respectively, and the photocurrents of 23.2 mA/cm^2 integrated from area of IPCE spectrum is consistent with the J_{sc} values obtained from the *J-V* curve. The onset of IPCE photocurrent is redshifted to ~900nm in comparison to polycrystalline PSCs, consistent with absorption spectra in Fig. 4. Finally, we note that PCE of 8.78% is accomplished without full coverage of single crystalline $CH_3NH_3PbI_3$ on FTO/TiO_2 substrate, as observed from two SEM images in Fig. S3. If fully covered on FTO/TiO_2 substrate, then PCE of the single crystalline PSCs is expected to be further enhanced, and there is much room for improvement. With continuous optimization of materials processing and device optimization, we fully expect that single crystalline PSCs will rival their polycrystalline counterpart in the foreseeable future.

Conclusion

Single crystalline $CH_3NH_3PbI_3$ has superior photovoltaic properties, though its integration into PSC device architecture is challenging. We overcame this difficulty by self-growing high quality single crystalline $CH_3NH_3PbI_3$ directly on polycrystalline FTO/TiO_2 substrate, as confirmed by X-ray diffraction and HRTEM. n-i-p type of PSC devices have been successfully fabricated, exhibiting maximum short-circuit current density of 24.40 mA/cm^2 and PCE of 8.78%, thanks to the smaller optic band gap and longer carrier life time of single crystals

as well as highly efficient charge extraction at $TiO_2/CH_3NH_3PbI_3$ interface. We note that the single crystalline $CH_3NH_3PbI_3$ does not fully cover the FTO/ TiO_2 substrate yet, and there is still much room for improvement. With continuous optimization of materials processing and device optimization, we fully expect that single crystalline PSCs will rival their polycrystalline counterpart in the foreseeable future.

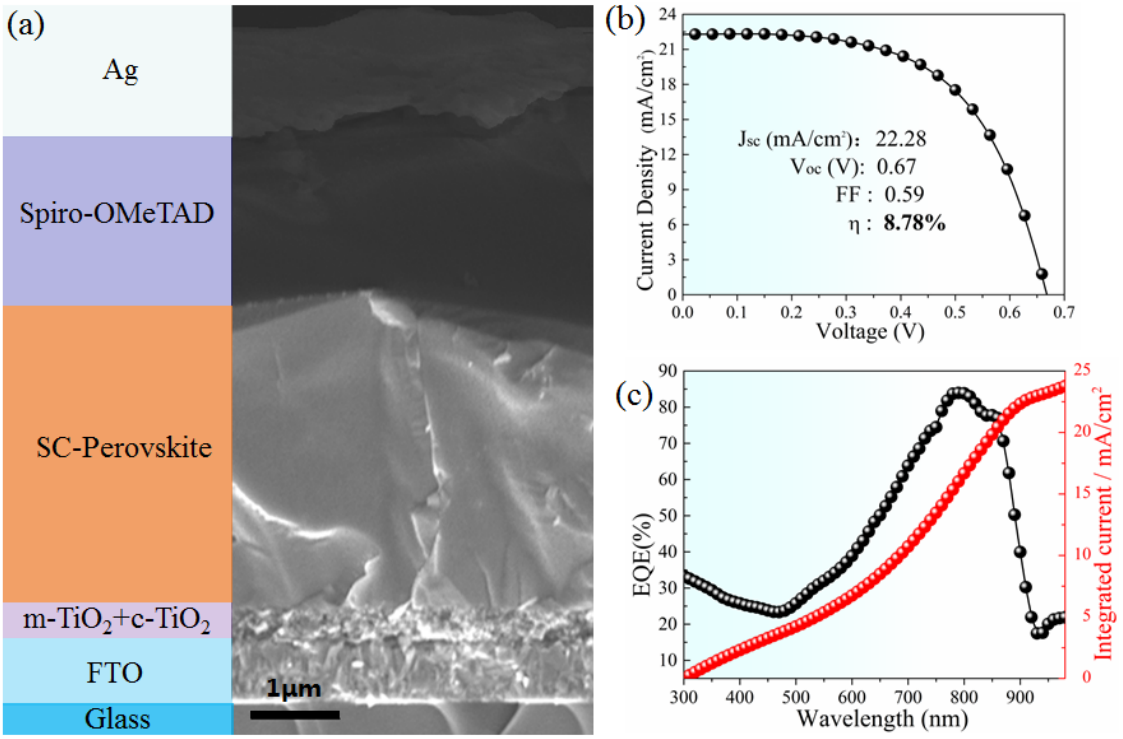

Fig. 5 Solar cell performance of single crystalline $CH_3NH_3PbI_3$. **a** Cross-section SEM image of the solar cell. **b** *J-V* curve. **c** IPCE.

Acknowledgement

We thank the support from National Key Research and Development Program of China (2016YFA0201001, 2016YFA0300804), National Natural Science Foundation of China (11627801, 51102172, 51672007, 51502007), the Leading Talents Program of Guangdong Province (2016LJ06C372), Shenzhen Science and Technology Innovation Committee (JCYJ20170307165905513,

JCYJ20170413152832151), Natural Science Foundation for Outstanding Young Researcher in Hebei Province (E2016210093), The Key Program of Educational Commission of Hebei Province of China (ZD2016022), The Youth Top-notch Talents Supporting Plan of Hebei Province. This research used resources of the Advanced Photon Source, a U.S. Department of Energy (DOE) Office of Science User Facility operated for the DOE Office of Science by Argonne National Laboratory under Contract No. DE-AC02-06CH11357.

References

1. Kojima A, Teshima K, Shirai Y et al (2009) Organometal halide perovskites as visible-light sensitizers for photovoltaic cells. J Am Chem Soc 131:6050–6051
2. Stranks SD, Snaith HJ (2015) Metal-halide perovskites for photovoltaic and light-emitting devices. Nat Nanotechnol 10:391–402
3. Wang Q, Chen HG, Liu G et al (2015) Control of organic-inorganic halide perovskites in solid-state solar cells: a perspective. Sci Bull 60:405–418
4. Fang R, Zhang WJ, Zhang SS et al (2016) The rising star in photovoltaics-perovskite solar cells: The past, present and future. Sci China Technol Sci 59:989–1006
5. Lee MM, Teuscher J, Miyasaka T et al (2012) Efficient hybrid solar cells based on meso-superstructured organometal halide perovskites. Science 338:643–647
6. Burschka J, Pellet N, Moon SJ et al (2013) Sequential deposition as a route to high-performance perovskite-sensitized solar cells. Nature 499:316–319
7. Zhou HP, Chen Q, Li G et al (2014) Interface engineering of highly efficient perovskite solar cells. Science 345:542–546
8. Chen W, Wu YZ, Yue YF et al (2015) Efficient and stable large-area perovskite solar cells with inorganic charge extraction layers. Science 350:944–948
9. Sha WEI, Ren XG, Chen LZ et al (2015) The efficiency limit of $CH_3NH_3PbI_3$ perovskite solar cells. Appl Phys Lett 106:221104

10. Shi D, Adinolfi V, Comin R et al (2015) Low trap-state density and long carrier diffusion in organolead trihalide perovskite single crystals. Science 347:519–522

11. Dong QF, Fang YJ, Shao YC et al (2015) Electron-hole diffusion lengths > 175 um in solution-grown $CH_3NH_3PbI_3$ single crystals. Science 347:967–970

12. Zhang FY, Yang B, Mao X et al (2017) Perovskite $CH_3NH_3PbI_{3-x}Br_x$ single crystals with charge-carrier lifetimes exceeding 260 μs. ACS Appl Mater Interfaces 9:14827–14832

13. Rao HS, Li WG, Chen BX et al (2017) In situ growth of 120 cm^2 $CH_3NH_3PbBr_3$ perovskite crystal film on FTO glass for narrowband-photodetectors. Adv Mater 29**:**1602639

14. Liu YC, Ren XD, Zhang J et al (2017) 120 millimeter single-crystalline perovskite and wafers: to-wards viable applications. Sci China Chem doi:10.1007/s11426-017-9081-3

15. Wang GM, Li DH, Cheng HC et al (2015) Wafer-scale growth of large arrays of perovskite microplate crystals for functional electronics and optoelectronics. Sci Adv 1:e1500613

16. Rao HS, Chen BX, Wang XD et al (2017) A micron-scale laminar $MAPbBr_3$ single crystal for an efficient and stable perovskite solar cell. Chem Commun 53:5163–5166.

17. Etgar L, Gao P, Xue ZS et al (2012) Mesoscopic $CH_3NH_3PbI_3/TiO_2$ heterojunction solar cells. J Am Chem Soc 134:17396–17399

18. Wang P, Zhao JJ, Liu JX et al (2017) Stabilization of organometal halide perovskite films by SnO_2 coating with inactive surface hydroxyl groups on ZnO nanorods. J Power Sources 339:51–60

19. Kutes Y, Ye LH, Zhou YY et al (2014) Direct observation of ferroelectric domains in solution-processed $CH_3NH_3PbI_3$ perovskite thin films. J Phys Chem Lett 5:3335–3339

20. Wang PQ, Zhao JJ, Wei LY et al (2017) Photo-induced ferroelectric switching in perovskite $CH_3NH_3PbI_3$ films. Nanoscale 9:3806–3817

21. Holger R, Tobias L, Michael JH et al (2017) Ferroelectric domains in methylammonium

lead iodide perovskite thin-films. Energy Environ Sci doi:10.1039/C7EE00420F

22. Strelcov E, Dong QF, Li T et al (2017) $CH_3NH_3PbI_3$ perovskites: ferroelasticity revealed. Sci Adv 3:e1602165

23. Stoumpos CC, Malliakas CD, Kanatzidis MG (2013) Semiconducting tin and lead iodide perovskites with organic cations: phase transitions, high mobilities, and near-infrared photoluminescent properties. Inorg Chem 52:9019–9038

24. Huang JS, Shao YC, Dong QF (2015) Organometal trihalide perovskite single crystals: a next wave of materials for 25% efficiency photovoltaics and applications beyond? J Phys Chem Lett 6:3218–3227

25. Chen Y, Yi HT, Wu X et al (2016) Extended carrier lifetimes and diffusion in hybrid perovskites revealed by hall effect and photoconductivity measurements. Nat Commun 7:12253

26. Zhao JJ, Wang P, Liu ZH et al (2015) Controlled reaction for improved $CH_3NH_3PbI_3$ transition in perovskite solar cells. Dalt Trans 44:17841–17849

27. Im JH, Jang IH, Pellet N et al (2014) Growth of $CH_3NH_3PbI_3$ cuboids with controlled size for high-efficiency perovskite solar cells. Nat Nanotechnol 9:927–932

28. Zhu ZL, Bai Y, Zhang T et al (2014) High-performance hole-extraction layer of sol–gel-processed nio nanocrystals for inverted planar perovskite solar cells. Angew Chemie 126:12779–12783

29. Zhong D, Cai B, Wang XL et al (2015) Synthesis of oriented TiO_2 nanocones with fast charge transfer for perovskite solar cells. Nano Energy 11:409–418

30. Fei CB, Li B, Zhang R et al (2017) Highly efficient and stable perovskite solar cells based on monolithically grained $CH_3NH_3PbI_3$ film. Adv Energy Mater 7:1602017